Vortex-induced three-degree-of-freedom vibration of a piggyback circular cylinder system

L.F. Chen[a], G.X. Wu[b,*]

[a]*School of Naval Architecture and Ocean Engineering, Jiangsu University of Science and Technology, China*
[b]*Department of Mechanical Engineering, University College London, Torrington Place, London WC1E7JE, UK*

Abstract

A stabilized finite element method is adopted to solve the Navier-Stokes equations written in the arbitrary Lagrangian-Eulerian from. Extensive simulations are undertaken to investigate the vortex induced vibration characteristics of a piggyback circular cylinder system, or a smaller cylinder rigidly connected to a main one. In particular, the system is in three-degree-freedom motion, or its rotation motion is taken into account, while the previous work very much focuses on translational motions. This is achieved though using remeshing during the motion of the system. Various case studies have been undertaken at Reynolds number $Re = 100$, as the prime purpose is not about turbulence itself but the effect of rotation on the interaction of the piggyback cylinder system with the flow. Extensive results are provided to show the motion behaviours of the piggyback system at different orientation relative to the incoming flow. The effect of the rotational motion is extensively investigated. Key physical features are highlighted and conclusions are then drawn.

Keywords: Piggyback circular cylinder system; 3DOF vortex induced vibration; Motion amplitude branch; ALE method; Stabilized FEM.

1. Introduction

Circular cylinders are widely adopted in ocean engineering, e.g., marine pipelines and risers, which are used for oil and gas transportation. To monitor oil loss or the amount of oil remaining in the pipelines, a small pipe is often bound to the primary pipeline, which is commonly called piggyback configuration[1]. In this way, the primary pipeline carries oil or gas; the small pipeline serves as an addendum for hydraulic fluid control or signal transmission, and the pipeline system is able to address the problem of oil loss and improve the economic efficiency of oil fields[2, 3].

In engineering practices, hydrodynamic loads of the piggyback pipeline system used for dynamic response analysis were often assessed using an "equivalent pipeline diameter approach. The approach assumes that hydrodynamic loads on the piggyback pipeline system are equal to those on a single pipeline with diameter equal to the projected height of the piggyback bundle (the sum of diameters of the large, small pipelines and spacing between them)[4, 5]. In fact, the flow past two pipelines in the piggyback configuration is more complex than that past a single pipeline, and its hydrodynamic load is different from that of a single pipeline. In the past few decades, although the interaction between flow and multiple cylinders of different diameters has been extensively investigated, systematic investigations into vortex-induced vibration response of two bundled circular cylinders in three-degree-of-freedom (3DOF) are still lacking.

A number of studies on flow characteristics and vortex shedding suppression past two stationary cylinders of different diameters have been undertaken. Strykowski and Sreenivasan (1990)[6] conducted a study on the formation and suppression of vortex shedding over a range of Reynolds numbers and found that vortex shedding behind circular cylinders could be altered or suppressed altogether by a proper placement of a second and much smaller cylinder in the near wake of the main cylinder. Sakamoto and Haniu (1994)[7], Tsutsui *et al.* (1997)[8], Dalton *et al.* (2001)[9] simulated the suppression of lift force on the main circular cylinder by a small one. Zhao *et al.* (2005)[10] carried out a numerical study of flow around two cylinders of different diameters at Reynolds number $Re = 500$. The effects of the small

---

cylinder on the flow around and forces on the two cylinders were investigated for different gap ratios and position angles at a diameter ratio of 0.25. Zhao *et al.* (2007)[11] and Zhao (2012)[12] studied the interaction between flow and two circular cylinders of different diameters at high Reynolds numbers in the subcritical regime. They found that only one vortex street was formed behind the cylinders if the two cylinders were very close to each other. Another vortex shedding mode was the interaction-shedding mode, in which the vortex shedding behind the cylinders was strongly affected by the shear layers behind the gap. Zang *et al.* (2013)[13] carried out swirling strength analysis of vortex shedding from near-bed piggyback pipelines in a steady incoming flow. They found that the lee-wake patterns for the near-bed piggyback pipelines were dependent on the configuration, including the ratio gap G between the cylinder bottom and seabed to diameter of the main cylinder D, or G/D, the ratio of spacing S between two cylinders to diameter, S/D, and the diameter ratio of two cylinders d/D. It was also reported in their work that the vortex shedding from the pipeline system was suppressed due to the existence of the small pipe with certain configurations.

There are also studies on the vortex-induced vibration (VIV) response of two circular cylinders of different diameters. Zhao and Yan (2013)[14] carried out a numerical simulation on two-degree-freedom VIV for two circular cylinders with $S/D = 0$ and 0.2 at Reynolds number $Re = 250$. The effect of the position angle of the small cylinder on the lock-in regime of the VIV was investigated. They reported that compared with a single cylinder case, the lock-in regime of the reduced velocity (U^*) was widened at some position angles. They also found that the lock-in regime in terms of the reduced velocity at $S/D = 0.2$ was narrower than that at $S/D = 0$ for all the position angles and the vibration amplitude at $S/D = 0.2$ was smaller than that at $S/D = 0$. Zang and Gao (2014)[15] conducted a series of experiments to investigate configuration effects on the VIV suppression of the near-bed piggyback pipelines. The effects of the mass-damping parameter, diameter ratio, gap-to-diameter ratio, spacing-to-diameter ratio and position angle of the small cylinder were taken into consideration. They indicated that the configuration parameters of piggyback pipelines had significant effect on the VIV suppression. When the small pipe stayed above the main pipe, the minimum peak amplitude occurred at $S/D \approx 0.25$. For a constant value of $S/D = 0.25$, the minimum peak amplitude occurred at a position angle around 120°.

In practical situations, the piggyback pipeline system in the flow may also rotate when in translational motions. The rotation of the system may influence the vortex shedding in the wake, which in turn affects the motion responses of the system. The present study takes the rotation of the piggyback pipeline system into account and undertakes further investigation of its effects on the VIV responses of the system. The study is conducted through numerical simulation using the stabilized finite element method for the Navier-Stokes equation in arbitrary Lagrangian-Eulerian form. The focus at this stage is not turbulence and therefore direct simulation (DNS) is adopted to solve the equations at a relatively low Reynolds number $Re = 100$. In such a case, the flow is very much purely two dimensional [16]. This allows us to focus on the VIV responses of the piggyback pipeline system in 3DOF, taking into account rotation in particular.

2. Mathematical model and numerical method

Vortex-induced vibration of a piggyback circular cylinder system is illustrated in Figure 1. A Cartesian coordinate system O-xyz is defined with the origin O at the centre of main cylinder and x in the direction of incoming flow and y pointing upwards. The main and small cylinders have diameters D and d respectively. The line linking the centres of the two cylinders forms an initial angle α with x axis, and S is distance between the intersection points of this line with the surfaces of two cylinders. These two cylinders are assumed to be rigidly connected and the system is in 3DOF motion under fluid loading. They are defined through the translational displacement X of the centre of the main cylinder and the rotational displacement θ about the centre.

2.1. Governing equations of the fluid

The fluid is assumed to be Newtonian and incompressible. The velocity (U_∞) of the incoming flow, the diameter of the main circular cylinder (D) and fluid density (ρ) are used for nondimensionalisation. In the arbitrary Lagrangian-Eulerian (ALE) form, the continuity and Navier-Stokes equations can be respectively written as[17]

$$\nabla \cdot \boldsymbol{u} = 0, \tag{1}$$

$$\mathcal{L}(\boldsymbol{u}, p; \boldsymbol{u}_m) = \frac{\partial \boldsymbol{u}}{\partial t} + ((\boldsymbol{u} - \boldsymbol{u}_m) \cdot \nabla) \boldsymbol{u} + \nabla p - \frac{2}{Re} \nabla \cdot (\nabla^s \boldsymbol{u}) = \boldsymbol{0}, \tag{2}$$
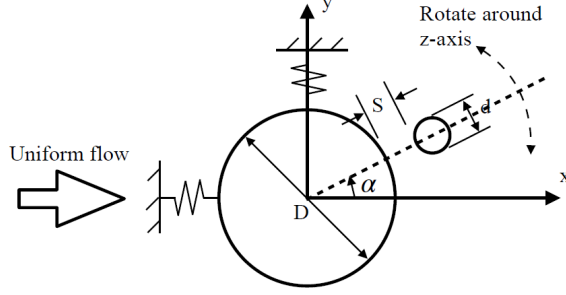
2

Figure 1: Sketch of piggyback circular cylinder system: translational motions in x- and y-axis and rotation around z-axis.

where $\boldsymbol{u}$ denotes the velocity vector, $\boldsymbol{u}_m$ is the mesh velocity, p represents the pressure, $Re = \rho U_\infty D/\mu$ denotes Reynolds number with μ being the dynamic viscosity, and $\nabla^s \boldsymbol{u} = (\nabla \boldsymbol{u} + (\nabla \boldsymbol{u})^T)/2$. The temporal derivative in Eq.(2) is taken in the moving mesh of velocity $\boldsymbol{u}_m$.

2.2. Stabilized finite element method

The finite element method is used to solve the above equations. To eliminate non-physical instabilities in the computation, it is combined with streamline-upwind Petrov-Galerkin (SUPG)[18], pressure-stabilizing Petrov-Galerkin (PSPG)[19, 20] and least-square stabilization for the incompressibility constraint (LSIC)[21, 22, 23]. Let the computational domain Ω be discretized into n_{el} elements and its boundary Γ into n_{eb} faces. Through Galerkin method, Eqs.(1) and (2) can be written as[24]

$$(q, \nabla \cdot \boldsymbol{u}^h)_\Omega + (q, \nabla \cdot \boldsymbol{u}')_\Omega = 0, \quad (3)$$

$$\left(\boldsymbol{w}, \frac{\partial \boldsymbol{u}^h}{\partial t} + (\boldsymbol{u} - \boldsymbol{u}_m) \cdot \nabla \boldsymbol{u}^h + \nabla p^h - \frac{2}{Re} \nabla \cdot (\nabla \boldsymbol{u}^h)\right)_\Omega + (\boldsymbol{w}, (\boldsymbol{u} - \boldsymbol{u}_m) \cdot \nabla \boldsymbol{u}')_\Omega + (\boldsymbol{w}, \nabla p')_\Omega = 0, \quad (4)$$

where $\boldsymbol{u}^h$ represents the discrete solution to Eqs. (1) and (2), q and w are the weighting functions for the continuity and momentum equations respectively, $(,)_\Omega$ represents integration of the inner product in the discretized computational domain, and[25, 26, 27]

$$\boldsymbol{u}' = -\boldsymbol{\tau}_m \mathcal{L}(\boldsymbol{u}^h, p^h; \boldsymbol{u}_m), \quad (5)$$

$$p' = -\tau_c \nabla \cdot \boldsymbol{u}^h, \quad (6)$$

Following the SUPG and LSIC methods, $\boldsymbol{\tau}_m$ and τ_c in the above equations are defined as follows[28, 29, 30]

$$\tau_m = \left(c_1(\boldsymbol{u}^h - \boldsymbol{u}_m)\boldsymbol{G}(\boldsymbol{u}^h - \boldsymbol{u}_m) + \frac{c_2}{Re^2}\boldsymbol{G} : \boldsymbol{G} + \frac{c_3}{\Delta t^2}\right)^{-\frac{1}{2}} \quad (7)$$

$$\tau_c = \frac{\boldsymbol{u}^h \boldsymbol{G} \boldsymbol{u}^h}{tr(\boldsymbol{G})} \quad (8)$$

where c_1, c_2 and c_3 are constants depending on the element type, which, for bilinear shape functions used in this paper, are taken as $c_1 = 4$, $c_2 = 36$ and $c_3 = 4$[31], $\boldsymbol{G}$ is a covariant metric tensor of the gradient of local element spatial coordinates ξ with respect to the global coordinates x for the same point

$$\boldsymbol{G} = \left(\frac{\partial \boldsymbol{\xi}}{\partial \boldsymbol{x}}\right)^T \frac{\partial \boldsymbol{\xi}}{\partial \boldsymbol{x}},$$

and $\partial \boldsymbol{\xi}/\partial \boldsymbol{x}$ is the Jacobian matrix, $\boldsymbol{G} : \boldsymbol{G}$ denotes a double dot product of $\boldsymbol{G}$ with $\boldsymbol{G}$, $tr(\boldsymbol{G})$ represents a summation of the diagonal of $\boldsymbol{G}$.

3

Through integration by parts, Eqs. (3) and (4) become

$$(q, \nabla \cdot \boldsymbol{u}^h)_\Omega - (\nabla q, \boldsymbol{u}')_\Omega + (q, \boldsymbol{u}')_\Gamma = 0, \qquad (9)$$

$$\left(\boldsymbol{w}, \frac{\partial \boldsymbol{u}^h}{\partial t} + (\boldsymbol{u}^h - \boldsymbol{u}_m) \cdot \nabla \boldsymbol{u}^h + \nabla p^h - \frac{2}{Re} \nabla \cdot (\nabla \boldsymbol{u}^h)\right)_\Omega$$
$$- \left((\boldsymbol{u}^h - \boldsymbol{u}_m) \cdot \nabla \boldsymbol{w}, \boldsymbol{u}'\right)_\Omega - (\nabla \cdot \boldsymbol{w}, p')_\Omega + \left((\boldsymbol{u}^h - \boldsymbol{u}_m) \cdot \boldsymbol{n}\boldsymbol{w}, \boldsymbol{u}'\right)_\Gamma + (\boldsymbol{w}, p'\boldsymbol{n})_\Gamma = 0, \qquad (10)$$

where $\boldsymbol{u}' = 0$ and $p' = 0$ at the boundary are used. Substituting the expression of $\boldsymbol{u}'$ and p' and rearranging Eqs. (9) and (10) yields

$$\left(q + \nabla \cdot \boldsymbol{w}\tau_c, \nabla \cdot \boldsymbol{u}^h\right)_\Omega = 0, \qquad (11)$$

$$\left((\boldsymbol{w} + (\boldsymbol{u}^h - \boldsymbol{u}_m) \cdot \nabla \boldsymbol{w}\tau_m + \nabla q^h \tau_m), \frac{\partial \boldsymbol{u}^h}{\partial t} + ((\boldsymbol{u}^h - \boldsymbol{u}_m) \cdot \nabla) \boldsymbol{u}^h + \nabla p^h - \frac{2}{Re} \nabla \cdot (\nabla^s \boldsymbol{u}^h)\right)_\Omega = 0, \qquad (12)$$

Eqs. (11) and (12) show that Eqs. (3) and (4) are equivalent to using modified weighting functions in the Galerkin method for the continuity and momentum equations respectively.

2.3. Equations of motion for the cylinder system

The free vibration of the piggyback circular cylinder system is modeled as a spring-mounted structure system. The rigid cylinder system is assumed to have mass m and rotational inertial I_{zz}, and is supported by a spring system. The system has damping c and stiffness k in the translations, and damping c_M and stiffness k_M in rotation. Without loss of generality, O may be assumed as the mass centre. The dimensionless 3DOF equations of the motion are given by

$$m^* \ddot{\boldsymbol{X}} + \frac{4\pi\zeta^*(m^*+1)}{U^{*2}} \dot{\boldsymbol{X}} + \frac{4\pi^2(m^*+1)}{U^{*2}} \boldsymbol{X} = \frac{2\boldsymbol{C}_F}{\pi}, \qquad (13)$$

$$I_{zz}^* \ddot{\theta} + \zeta_M^* \dot{\theta} + k_M^* \theta = \frac{2C_M}{\pi}, \qquad (14)$$

where $\boldsymbol{X} = \{X, Y\}$ denotes the in-line and transverse cylinder displacements relative to the initial position, the over dot denotes the derivative with respect to time t, $m^* = m/m_a$ is the ratio of cylinder system mass to the potential flow added mass $m_a = \rho\pi D^2/4$ of the main cylinder, $\zeta^* = c/(2\sqrt{k(m + m_a)})$ is damping ratio and $U^* = U_\infty/(f_n D)$ is reduced velocity with $f_n = \sqrt{k/(m + m_a)}/(2\pi)$ being natural frequency of the main cylinder in the potential flow, which is approximately the natural frequency of the cylinder system, I_{zz}^* denotes the dimensionless moment of inertia, ζ_M^* represents the damping ratio in rotation, k_M^* is the coefficient of restoring moment. The force coefficient $\boldsymbol{C}_F = \{C_D, C_L\}$ can be obtained from[32]

$$C_D = \frac{F_{D,1} + F_{D,2}}{0.5\rho U_\infty^2 D} = \int_0^{2\pi} \left[\left(-p + \frac{2}{Re}\frac{\partial u}{\partial x}\right)\cos\theta_1 + \frac{1}{Re}\left(\frac{\partial u}{\partial y} + \frac{\partial v}{\partial x}\right)\sin\theta_1\right] d\theta_1$$

$$+ \int_0^{2\pi} \left[\left(-p + \frac{2}{Re}\frac{\partial u}{\partial x}\right)\cos\theta_2 \frac{d}{D} + \frac{1}{Re}\left(\frac{\partial u}{\partial y} + \frac{\partial v}{\partial x}\right)\sin\theta_2 \frac{d}{D}\right] d\theta_2$$

$$C_L = \frac{F_{L,1} + F_{L,2}}{0.5\rho U_\infty^2 D} = \int_0^{2\pi} \left[\left(-p + \frac{2}{Re}\frac{\partial u}{\partial x}\right)\sin\theta_1 + \frac{1}{Re}\left(\frac{\partial u}{\partial y} + \frac{\partial v}{\partial x}\right)\cos\theta_1\right] d\theta_1$$

$$+ \int_0^{2\pi} \left[\left(-p + \frac{2}{Re}\frac{\partial u}{\partial x}\right)\sin\theta_2 \frac{d}{D} + \frac{1}{Re}\left(\frac{\partial u}{\partial y} + \frac{\partial v}{\partial x}\right)\cos\theta_2 \frac{d}{D}\right] d\theta_2, \qquad (15)$$

4

where θ_1 and θ_2 are the angles around the centres of the larger and smaller cylinders in the polar coordinate systems respectively. The rotational moment coefficient C_M in Eq.(14) can be obtained from

$$C_M = \frac{M_f}{0.5\rho U_\infty^2 D^2} = \int_0^{2\pi} \left[\left(-p + \frac{2}{Re}\frac{\partial u}{\partial x}\right)\cos\theta_1 + \frac{1}{Re}\left(\frac{\partial u}{\partial y} + \frac{\partial v}{\partial x}\right)\sin\theta_1 \right] y_e \mathrm{d}\theta_1$$

$$- \left[\left(-p + \frac{2}{Re}\frac{\partial u}{\partial x}\right)\sin\theta_1 + \frac{1}{Re}\left(\frac{\partial u}{\partial y} + \frac{\partial v}{\partial x}\right)\cos\theta_1 \right] x_e \mathrm{d}\theta_1$$

$$+ \int_0^{2\pi} \left[\left(-p + \frac{2}{Re}\frac{\partial u}{\partial x}\right)\cos\theta_2\frac{d}{D} + \frac{1}{Re}\left(\frac{\partial u}{\partial y} + \frac{\partial v}{\partial x}\right)\sin\theta_2\frac{d}{D} \right] y_e \mathrm{d}\theta_2$$

$$- \left[\left(-p + \frac{2}{Re}\frac{\partial u}{\partial x}\right)\sin\theta_2\frac{d}{D} + \frac{1}{Re}\left(\frac{\partial u}{\partial y} + \frac{\partial v}{\partial x}\right)\cos\theta_2\frac{d}{D} \right] x_e \mathrm{d}\theta_2, \tag{16}$$

where $\boldsymbol{x}_e = \{x_e, y_e\}$ is the non-dimensionalized position vector relative to the rotational centre (the centre of the larger cylinder) from the surface of the larger or smaller cylinder.

2.4. Moving mesh

In the computation, an initial mesh is first generated. The subsequent mesh is obtained by moving the nodal points of the initial mesh according to the body motion without changing the mesh topology. The displacements of the nodal points at each time step are calculated using the following equation[11]

$$\nabla \cdot (\frac{1}{A_e}\nabla\boldsymbol{\eta}) = 0 \tag{17}$$

where $\boldsymbol{\eta}$ represents the displacements of the nodal points, A_e denotes the area of the element. Eq. (17) is solved using standard finite element method with given boundary conditions. When the Galerkin method is applied to Eq.(17), integration by parts is used. Then the spatial integration is performed element by element. Within each element, A_e is a constant.

3. Time stepping

A generalized-α method[33] is employed to advance Eq. (12) in time. Re-arranging the equation in terms of the temporal derivative and the rest yields the following equation

$$M\dot{\boldsymbol{a}} = N\boldsymbol{a}. \tag{18}$$

where $\boldsymbol{a}$ is the vector of variables $\{\boldsymbol{u}, p\}^T$ at discrete nodes, $\dot{\boldsymbol{a}}$ represents their temporal derivative, M is a 3×3 diagonal matrix with $M_{33} = 0$ and M_{jj} (j=1,2) are obtained from the integral of product of the weight function and shap function of $\partial \boldsymbol{u}/\partial t$. N_{ij} (i, j=1,2) are comprised of the parametric coefficients of the nonlinear convection and diffusion terms in Eq. (12). N_{i3}(i=1,2) is related to the pressure terms, N_{3j}(j=1,2) is related to Eq. (11) and $N_{33} = 0$. Using the generalized-α method, the advance from step n to step $n + 1$ can be obtained from the following equations

$$\boldsymbol{R}(\dot{\boldsymbol{a}}_{n+\alpha_m}, \boldsymbol{a}_{n+\alpha_f}) = M\dot{\boldsymbol{a}}_{n+\alpha_m} - N\boldsymbol{a}_{n+\alpha_f} = \boldsymbol{0}, \tag{19}$$

$$\boldsymbol{a}_{n+1} = \boldsymbol{a}_n + \Delta t\dot{\boldsymbol{a}}_n + \gamma\Delta t(\dot{\boldsymbol{a}}_{n+1} - \dot{\boldsymbol{a}}_n), \tag{20}$$

$$\dot{\boldsymbol{a}}_{n+\alpha_m} = \dot{\boldsymbol{a}}_n + \alpha_m(\dot{\boldsymbol{a}}_{n+1} - \dot{\boldsymbol{a}}_n), \tag{21}$$

$$\boldsymbol{a}_{n+\alpha_f} = \boldsymbol{a}_n + \alpha_f(\boldsymbol{a}_{n+1} - \boldsymbol{a}_n), \tag{22}$$

where α_m and α_f are set as

$$\alpha_m = \frac{1}{2}\left(\frac{3-\zeta}{1+\zeta}\right), \quad \alpha_f = \frac{1}{1+\zeta}, \tag{23}$$

and

$$\gamma = 0.5 + \alpha_m + \alpha_f, \tag{24}$$

ζ is set to 0.5 to allow the method to retain stability and a second-order accuracy[33]. The Newton-Raphson iterative procedure is used to solve the non-linear equations (19)-(22), as in Chen and Wu (2019)[24]. The matrix equation at each iteration is solved using a Generalized Minimum Residual
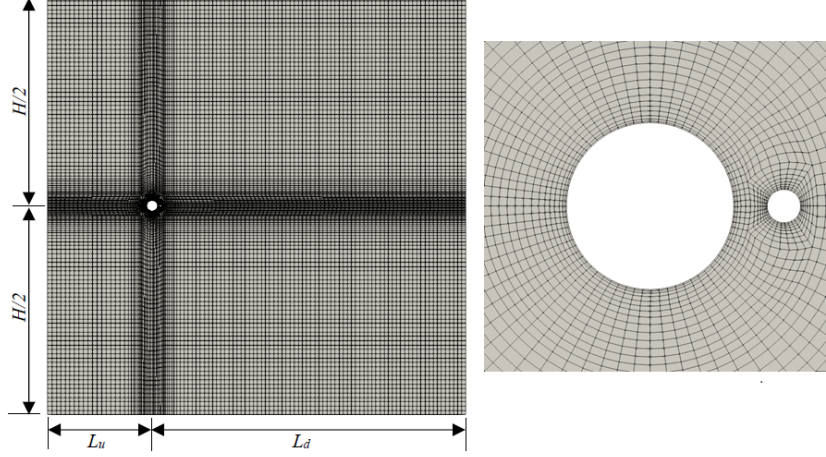
5

Figure 2: Sketch of computational domain and finite element mesh.

(GMRES) method with an absolute tolerance 1.0×10^{-8}. The tolerance for the Newton-Raphson iteration is set as 1.0×10^{-6}. Eqs. (13) and (14) are solved using a second-order Newmark-β method, as done in Chen and Wu (2020)[34, 35]. The algorithms for Eq. (13) are given as

$$m^* \ddot{\boldsymbol{X}}_{n+1} + \frac{4\pi\zeta(m^*+1)}{U^{*2}}\dot{\boldsymbol{X}}_{n+1} + \frac{4\pi^2(m^*+1)}{U^{*2}}\boldsymbol{X}_{n+1} = \frac{2\boldsymbol{C}_F^n}{\pi}, \tag{25}$$

$$\dot{\boldsymbol{X}}_{n+1} = \dot{\boldsymbol{X}}_n + \Delta t\left((1-\beta)\ddot{\boldsymbol{X}}_n + \beta\ddot{\boldsymbol{X}}_{n+1}\right), \tag{26}$$

$$\boldsymbol{X}_{n+1} = \boldsymbol{X}_n + \Delta t\dot{\boldsymbol{X}}_n + \frac{\Delta t^2}{2}\left((1-\beta)\ddot{\boldsymbol{X}}_n + \beta\ddot{\boldsymbol{X}}_{n+1}\right), \tag{27}$$

where $\beta = 0.5$. The algorithms of Eq. (14) are in the same form as Eq. (13).

4. Problem description

Simulations are performed in a rectangular computational domain using the above described numerical procedure. The inlet and outlet boundaries are located respectively at $L_u = 10D$ upstream and $L_d = 30D$ downstream of the centre of the main cylinder. The effects of the boundary truncations far upstream and downstream the cylinder can then be neglected (Prasanth *et al.* 2006[36]). The side boundary of the computational domain is symmetrically located at a distance of $20D$ from the centre of the cylinder, with which the effect of the blockage ratio of the computational domain is found to be insignificant.

The computational domain is discretized using a body-fitted mesh generated by ICEM CFD, in which quadrilateral elements are adopted and smaller cells are locally used near the body surface. A mesh sketch for the case $\alpha = 0^o$ is shown in Figure 2. Over each element, bilinear shape function is used for the velocity $\boldsymbol{u}$ and pressure p. It is also used for the weighting functions $\boldsymbol{w}$ and pressure q.

A uniform incoming flow with a constant velocity ($u^h = 1$, $v^h = 0$) is set as the boundary condition at the inlet. No slip boundary conditions are imposed on the solid surfaces of the smaller and larger cylinders, or

$$\begin{cases} u^h = \dot{X} + y_e\dot{\theta}, \\ v^h = \dot{Y} - x_e\dot{\theta}, \end{cases}$$

At the top and bottom sides of the domain, the normal velocity component $v^h = 0$ and the shear stress along the boundaries

$$\sigma_{xy} = \frac{1}{Re}\left(\frac{\partial u^h}{\partial y} + \frac{\partial v^h}{\partial x}\right) \tag{28}$$

is also set to be zero. At the outlet, the following boundary condition is employed[37]

$$-p^h\boldsymbol{n} + \mu\nabla^s\boldsymbol{u}^h \cdot \boldsymbol{n} - (\{\boldsymbol{u}^h \cdot \boldsymbol{n}\}_-)\boldsymbol{u}^h = \boldsymbol{0}, \tag{29}$$

6

where $\{\boldsymbol{u}^h \cdot \boldsymbol{n}\}_- = \min(0, \boldsymbol{u}^h \cdot \boldsymbol{n})$. The first two terms on the left-hand side in Eq. (29) are the normal stress, and the last term is related to the mass flow rate passing through the outlet. The latter is taken as zero when $\boldsymbol{u}^h \cdot \boldsymbol{n}$ is negative to prevent the reversed flow going into the computational domain.

In solving Eq. (17) for the node displacements, the boundary condition at the cylinder is set as

$$\boldsymbol{S}^T = \begin{bmatrix} \cos\theta & -\sin\theta \\ \sin\theta & \cos\theta \end{bmatrix} \cdot \begin{bmatrix} x_e \\ y_e \end{bmatrix} + \begin{bmatrix} X \\ Y \end{bmatrix} - \begin{bmatrix} x_e \\ y_e \end{bmatrix}, \tag{30}$$

For the mesh velocity $\boldsymbol{u}_m = \{u_m, v_m\}$, they can be obtained from $\boldsymbol{u}_m(t) = [\boldsymbol{X}_m(t) - \boldsymbol{X}_m(t - \Delta t)]/\Delta t$ to match the time stepping procedure. A fixed value of zero for u, v, or p is set for the other boundary conditions in solving Eq. (17).

5. Results and discussions

The FEM code developed in house using C++ is adopted as the numerical simulation tool, which has been successfully used to solve related problems[24, 38, 39].

5.1. Code validation

A single circular cylinder with $m^* = 10$, $\zeta^* = 0$ and $U^* = 4.92$ at $Re = 100$ is used as a test case to validate the computational procedure and the FEM code. The cylinder is in translation only. Three meshes with 9520, 15016 and 21187 cells and three time steps, which satisfy Courant-Friedrich-Lewy (CFL) condition $((u\Delta t/\Delta x)_{max} \leq 1$, Δx is the element size), are tested for the mesh and time step convergence. The obtained fluid force coefficients and other results are listed in Table 1. $\overline{C}_D$ represents the mean value of C_D, Y_{max}, $C_{L,max}$ and $C_{D,max}$ denote the maximum peak values of Y, C_L, C_D respectively, St is the nondimensional Strouhal number, and

$$X_{rms} = \left(\frac{1}{N} \sum_{n=1}^{N} (X^n - \overline{X})^2 \right)^{\frac{1}{2}}, \tag{31}$$

is the root-mean-square (RMS) value of displacement X, where N is the number of the discrete sample in time. The table shows that the results from the second and third meshes with $\Delta t = 0.025$ are in good agreement and that the results obtained using $\Delta t = 0.025$ and $\Delta t = 0.0125$ for the second mesh are the same for the first three figures after the piont, which indicates that the convergence has been achieved when the second mesh is used with $\Delta t = 0.025$. Comparisons are also made with the results from Singh and Mittal[40] and good agreement between the force coefficients can be seen. In the subsequent simulations, a similar number of cells to that of the second mesh is used together with $\Delta t = 0.025$.

Table 1: Mesh convergence study and comparison for a single circular cylinder ($m^* = 10$, $\zeta^* = 0$, $U^* = 4.92$ and $Re = 100$).

Number of cells	Δt	Y_{max}	$\overline{X}$	X_{rms}	$C_{L,max}$	$C_{D,max}$	$\overline{C}_D$	St
9520	0.0250	0.5760	0.0860	0.0040	0.940	2.810	2.210	0.1950
15016	0.0500	0.5747	0.0866	0.0060	0.946	2.847	2.224	0.1953
15016	0.0250	0.5800	0.0870	0.0060	0.950	2.860	2.230	0.1970
15016	0.0125	0.5806	0.0873	0.0061	0.950	2.860	2.230	0.1972
21187	0.0250	0.5820	0.0870	0.0070	0.950	2.870	2.232	0.1970
Singh and Mittal[40]		0.5700	0.0900	0.0100	0.960	3.010	2.380	0.2000

5.2. Motion response

In the case studies undertaken below, we have chosen $m^* = 10$, $d = S = 0.2D$, The Reynolds number is fixed at $Re = 100$. Seven configurations ($\alpha = 0^o$, 30°, 60°, 90°, 120°, 150° and 180°) of the piggyback cylinder system are considered. For each configuration, simulations are carried out at different reduced velocity U^*, which is achieved by changing the stiffness (k). In all the cases, the damping ratios in translation (ζ) and in rotation (ζ_M^*) are set to be zero, the moment of inertia and the restoring coefficient in rotation are fixed as $I_{zz}^* = 1.25$ and $k_M^* = 2.5$.

Motion trajectories of the rotational centre O of the system in 3DOF at different alpha are given in Figure 3. At each alpha, four different values of U^* have been considered. The first one is chosen at a
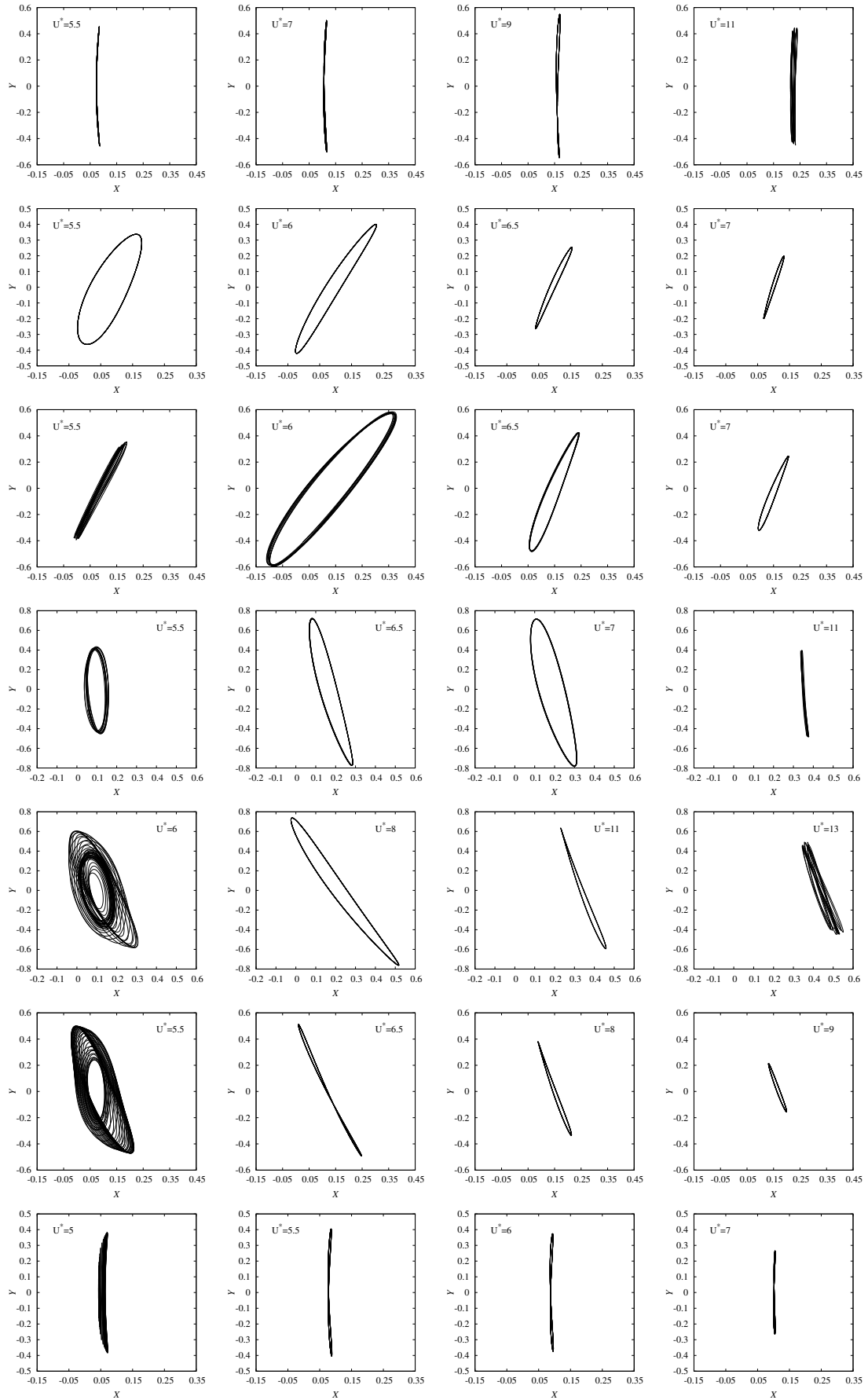
Figure 3: Motion trajectories of a piggyback circular cylinder system at $Re = 100$. From top to bottom: $\alpha = 0^o$, 30°, 60°, 90°, 120°, 150°, 180°.
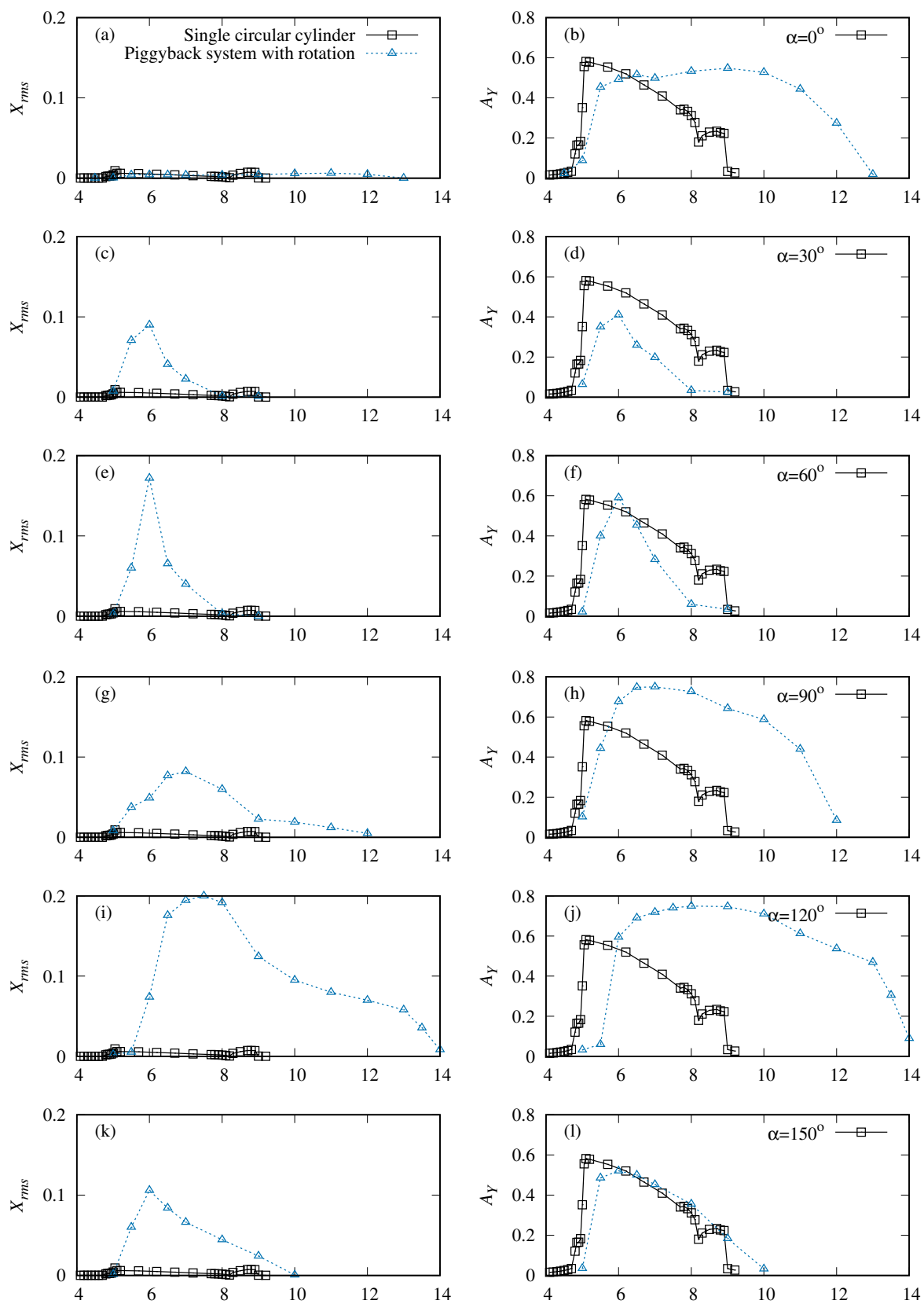
8

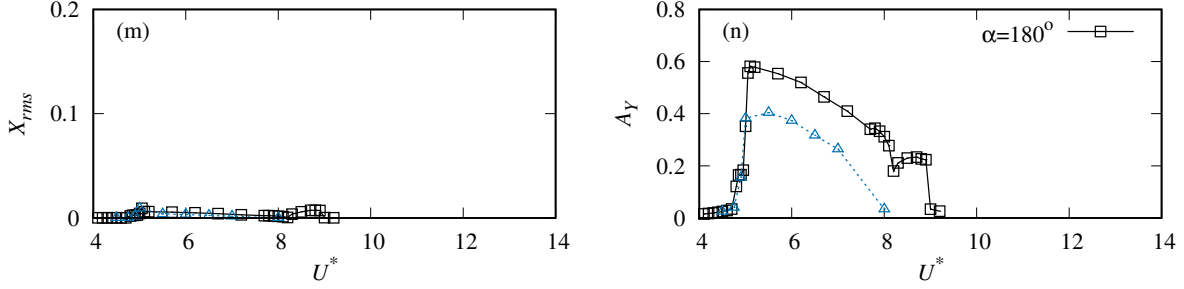Figure 4: Variations of in-line X_{rms} and transverse A_y against U^*. (Continued)

Figure 4: Variations of in-line X_{rms} and transverse A_y against U^*.

lower motion amplitude, the second at a higher amplitude and followed by two at a lower amplitude. It can be seen that in most cases the motion trajectory of the system eventually reaches a cyclical state, although hysteretic or non cyclical motion trajectories may occur for some U^* at each α, such as at $U^* = 5.5$ when $\alpha = 60^o$, $U^* = 6$ when $\alpha = 120^o$ and $U^* = 5.5$ when $\alpha = 150^o$. Specifically, when $\alpha = 0^o$(top row) or 180^o(bottom row), or when the system is in tandem arrangement, the motion trajectories take a form of a classical pattern of 8, and the dominant frequency f_x of in-line oscillation is twice f_y of the transverse oscillation, or $f_x = 2*f_y$, which is similar to that of two fixed identical cylinders in tandem (Jiao and Wu[41]). The narrow width of the 8 shape means that the motion amplitude in the X direction is much smaller than that in the Y direction. This behaviour is similar to that of a single cylinder. When $\alpha = 30^o$, the motion trajectory is a right-leaning closed curve. The trajectory at $U^* = 5.5$ resembles an oval. As U^* increases to 6, the oval becomes thinner. As U^* further increases to 6.5 and 7, the oval tends to a straight line while the motion amplitude decreases. When $\alpha = 60^o$, at $U^* = 5.5$, the trajectory is not a simple closed curve, showing non-cyclical motion. However the trajectory is within a narrow band of straight line. At $U^* = 6$, a wider oval shape can clearly be seen, showing a cyclical nature. At $U^* = 6.5$, the oval becomes thinner as well as shorter. Also noticed is that the top tip is narrower than the bottom tip. The oval becomes even thinner and shorter at $U^* = 7.5$. When $\alpha = 90^o$or two cylinders are side by side, at $U^* = 5.5$, the trajectory is almost a vertical oval. At $U^* = 6.5$, the oval becomes left-leaning. The oval becomes thinner and longer, and its bottom tip is narrower than the top tip, which is opposite to the case of $\alpha = 60^o$. At $U^* = 7$, the oval becomes wider again and at large value of $U^* = 11$, the trajectory becomes almost a straight line. At $\alpha = 120^o$, the trajectory becomes more left-leaning. At smaller U^*, it is non-cyclical. As U^* increases, it becomes more cyclical and the trajectory is confined in a narrow band of a straight line. This band becomes a bit wider and line becomes shorter as U^* increases. There is also a tendency of non-cyclical motion at larger U^*. When $\alpha = 150^o$, the trajectory is less left-leaning than $\alpha = 120^o$. The motion trajectory is non-cyclical at a smaller $U^* = 5.5$. When U^* increases, it becomes almost a straight line and the length of the line decreases as U^* increases. When $\alpha = 180^o$, or the cylinders in tandem arrangement, the trajectory is virtually a vertical line, indicating small motion in X direction. However there is some indication of non-cyclical motion at smaller $U^* = 5$.

Figure 4 shows the variations of X_{rms} and the amplitude of the transverse displacement ($A_Y = 0.5*(Y_{max} - Y_{min})$) against U^*, where Y_{min} is the minimum trough of Y. The corresponding results of a single circular cylinder of the same mass are also plotted for comparison. For a single cylinder, the in-line motion is small and the A_Y curve exhibits the typical three branch behaviour (Khalak and Williamson[42]). At small U^*, A_Y is small, which corresponds to the initial branch. As U^* increases to a particular value, which is defined as U_{IU}^* by Jiao and Wu (2021)[43], there is a rapid rise of A_Y, and the curve moves into the upper branch. When U^* continues to increase and reaches another critical value, defined as U_{UL}^* by Jiao and Wu (2021), A_Y decreases rapidly, and curve moves into lower branch. For the piggyback cylinder, the motion amplitude curve is very much affected by α. When $\alpha = 0^o$, the in-line motion is as small as the single cylinder. The A_Y curve shows a similar pattern of three branches. However, the variation at U_{IU}^* is less steep than that of the single cylinder or the piggyback system without rotation. In the upper branch, A_Y of the piggyback cylinder is generally larger than that of the single cylinder, and it remains significant over a wider range of U^*. Unlike the single cylinder, there is no clear point of U_{UL}^* where A_Y drops rapidly. Instead, at large U^*, A_Y decreases much more mildly. When $U^* > 9$, the motion of a single cylinder becomes small. However, the motion of the piggyback system remains noticeable until $U^* \approx 13$.

When $\alpha = 30^o$ or 60°, the motion trajectory of the piggyback cylinder system resembles a right-
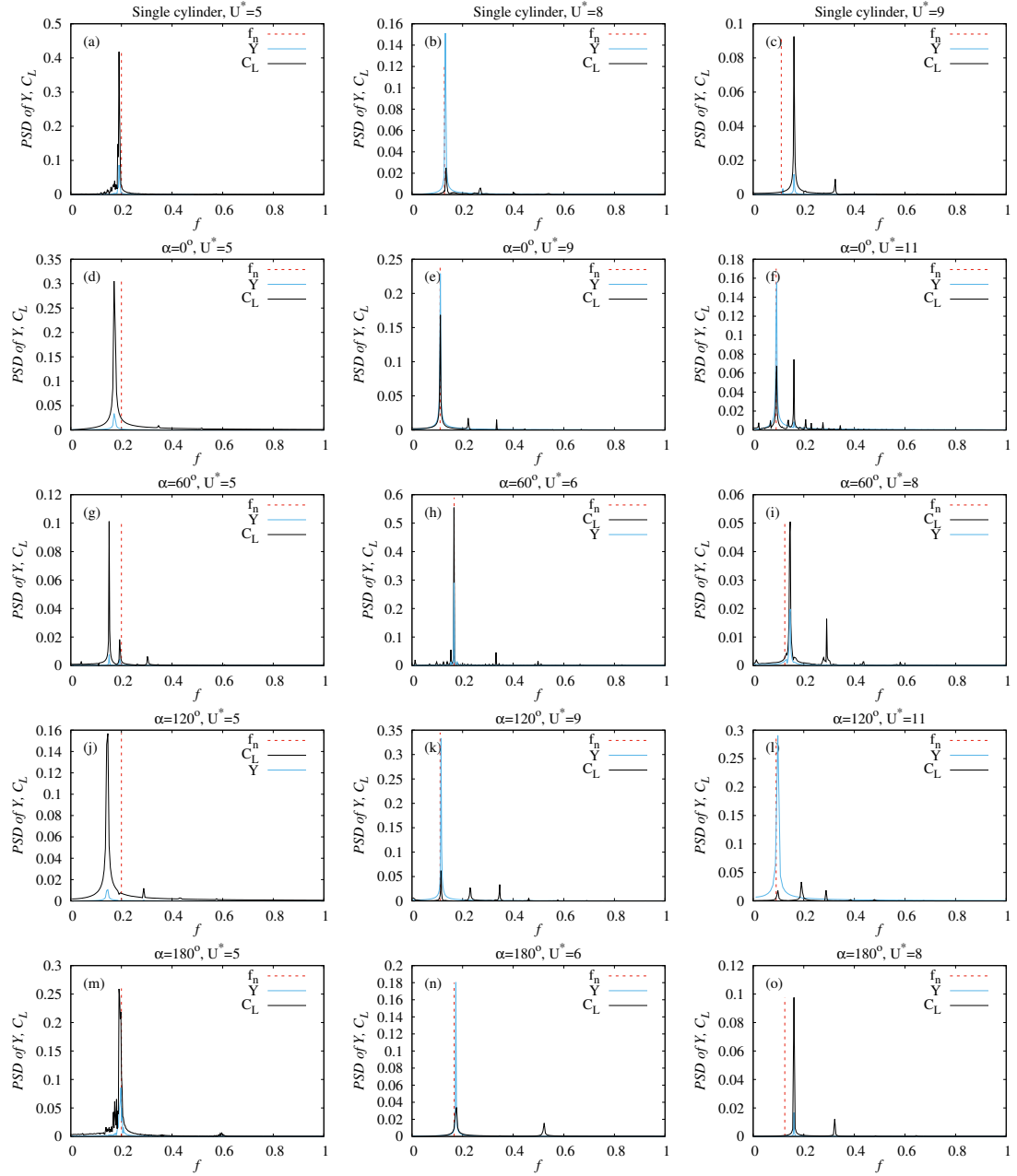
10

Figure 5: Power spectra density (PSD) profiles of the $Y(t)$ and $C_L(t)$ of the single circular cylinder and the piggyback cylinder system at $\alpha = 0^o$, 60°, 120° and 180°.

leaning oval within a range of U^*, as shown in Fig.3. Fig.4 shows that there is a peak of X_{rms} around $U^* \approx 6$ at both $\alpha = 30^o$ and 60°. Close to this value, the in-line motion is significant. The transverse motion is generally smaller than that of a single cylinder in these two arrangements. The transverse motion starts to increase significantly around U^*_{IU}, but much more mildly than a single cylinder. A_Y reaches a peak at $U^* \approx 6$. Unlike $\alpha = 0^o$ where the curve remains flatter around the peak for a while, the amplitude here declines almost immediately when U^* increases. The amplitude curve has only two branches instead of three. The second branch ends at smaller U^* than that at $\alpha = 0^o$.
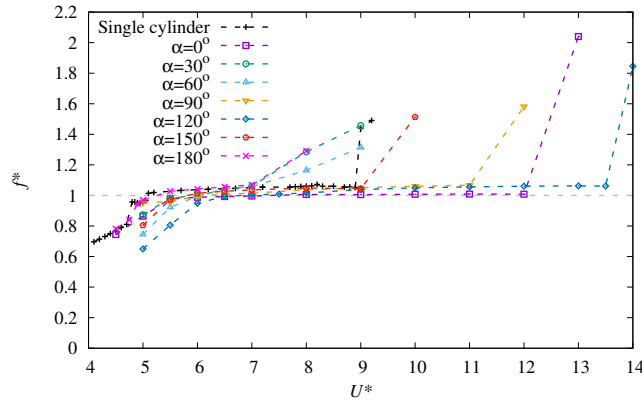
Figure 6: Profiles of the ratios ($f^* = f^*_y/f^*_n$) of the transverse oscillation frequencies (f^*_y) to the natural frequencies f^*_n of the system.

At $\alpha = 90^o$, or the system is in side by side arrangement, the peak of X_{rms} is smaller than that in the previous cases and its location is at a higher value $U^* \approx 7$. X_{rms} remains significant over a larger range of U^*. The shape of A_Y is similar to that at $\alpha = 0^o$, but has a larger value and therefore is much larger than that of the single cylinder at upper branch. When $\alpha = 120^o$, it is an amplified version of $\alpha = 90^o$. Both X_{rms} and A_Y become even larger and they become significant over a wider range of U^*. This pattern reverses at $\alpha = 150^o$. At $\alpha = 180^o$, or the reserved tandem arrangement, X_{rms} is very small. A_Y is much smaller than that of the tandem arrangement at $\alpha = 0^o$ and is even smaller than a single cylinder. The range of U^* within which A_Y is significant is also very much reduced.
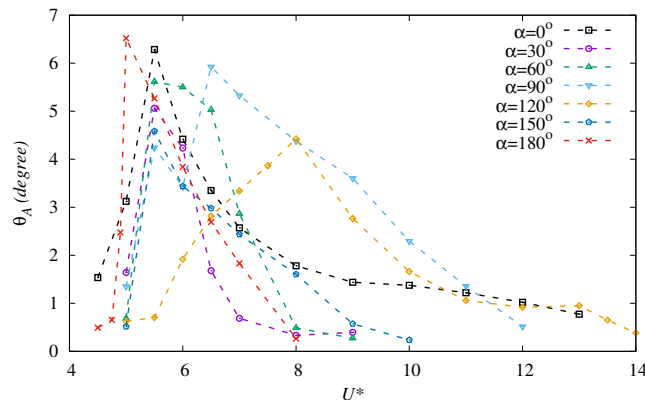

Figure 7: Rotation angle amplitude (θ_A) of the piggyback circular cylinder system at $Re = 100$.

The power spectra density (PSD) of $Y(t)$ obtained by performing Fourier analysis is shown in Figure 5 at different α together with that of the single cylinder. Three U^* have been chosen. The first one U^*_1 is taken around U^*_{IU}, the second one U^*_2 is around the peak value of A_Y and the third one U^*_3 is a larger value away from the peak of A_Y. The red dashed line in the figure is $f^*_n=1/U^*$, which is approximately the nondimensionalized natural frequency of the system. In all the cases calculated, at U^*_2, the dominant frequency f_y of $Y(t)$ is almost coincident with f^*_n. This means that when A_Y is around its peak, $f^*_y \approx f^*_n$, or near resonance. For the single cylinder at U^*_1, f^*_y is close to f^*_n, while at U^*_3, f^*_y is noticeably higher than f^*_n. For piggyback system at $\alpha = 0^o$ and 120°, f^*_y is smaller than f^*_n at U^*_1, while it is very close to f^*_n at U^*_2 and U^*_3. At $\alpha = 60^o$, f^*_y is smaller than f^*_n at U^*_1. It increases with U^* and is very similar

12

to f_n^* at U_2^* and then becomes larger than f_n^* at U_3^*. At $\alpha = 180^o$, it becomes similar to that of a single cylinder, $f_y^* \approx f_n^*$ at U_1^* and U_2^*, and noticeably larger than f_n^* at U_3^*.

Figure 6 shows the ratio of the dominant frequency f_y^* of $Y(t)$ to f_n^*, or $f^* = f_y^*/f_n^*$. The general trend for the single circular cylinder and the piggyback cylinder is that $f^* < 1$ at smaller U^*, then $f_* \approx 1$ when U^* increases and it will remain the case until a much larger value, where $f^* > 1$. For each configuration, $f^* \approx 1$ over a wide range of U^*, which indicates that the cylinder is approximately in resonance. This range is $4.8 \le U^* \le 8.9$ for the single cylinder. It is $5.5 \le U^* \le 7$ when $\alpha = 30^o$ and 60°, and is $5 \le U^* \le 7$ when $\alpha = 180^o$. The range at $\alpha = 150^o$ is similar to that of the single cylinder.

Figure 7 shows the rotation angle amplitude $\theta_A = 0.5(\theta_{max} - \theta_{min})$ of the piggyback cylinder system at different α, while the variation of its frequency f_M^* is the same as that in Figure 6. For all the configurations, the rotation angle amplitude first increases with U^*, reaches a peak and then decreases with U^*. Given $I_{zz}^* = 1.25$ and $k_M^* = 2.5$, the natural frequency of the rotation $f_{n,M}^* = \sqrt{k_M^*/\left(I_{zz}^* + \frac{I_{zz,a}}{m_a D^2}\right)}/(2\pi) = 0.2228$, where $I_{zz,a} = \rho \pi \frac{d^2}{2} l^2$ is the rotational added mass of the small cylinder about O and $l = 0.5D + S + 0.5d$. From Figure 6, we obtain that the f_M^* is in the range $0.07143 < f_M^* < 0.202$. $f_{n,M}^*$ is outside of this range and therefore the rotational motion is not in its own resonant motion, while the transverse motion is. Combined with the results of A_Y, it is noted that the location of the peak of θ_A is closely related to that of A_Y. From the figure, it can be observed that θ_A remains at the relatively large value in the range of $5 \le U^* \le 6.5$ when $\alpha = 0^0, 30^0, 60^0, 150^0$ or 180^0. When $\alpha = 90^0$ or 120^0, θ_A can be significant at larger U^*.

5.3. Hydrodynamic force

Figure 8 shows the RMS profiles of the drag ($C_{D,rms}$) and amplitude of the lift ($C_{L,A}$) coefficients of the piggyback system against U^*. Like the X_{rms} curve, the $C_{D,rms}$ curve increases first and then decreases with U^*. The $C_{L,A}$ curve of the single circular cylinder increases with U^* and rapidly reaches a peak at small U^*, which corresponds to the initial branch of the A_Y. As U^* continues to increase, it can be seen that $C_{L,A}$ starts to decrease with U^*. It can also be seen from Figure 4 that A_Y remains large at these U^* even if $C_{L,A}$ decreases. This phenomenon can be explained by the relationship between $C_{L,A}$ and A_Y. Considering the transverse motion of the system, $Y(t)$ takes the following form
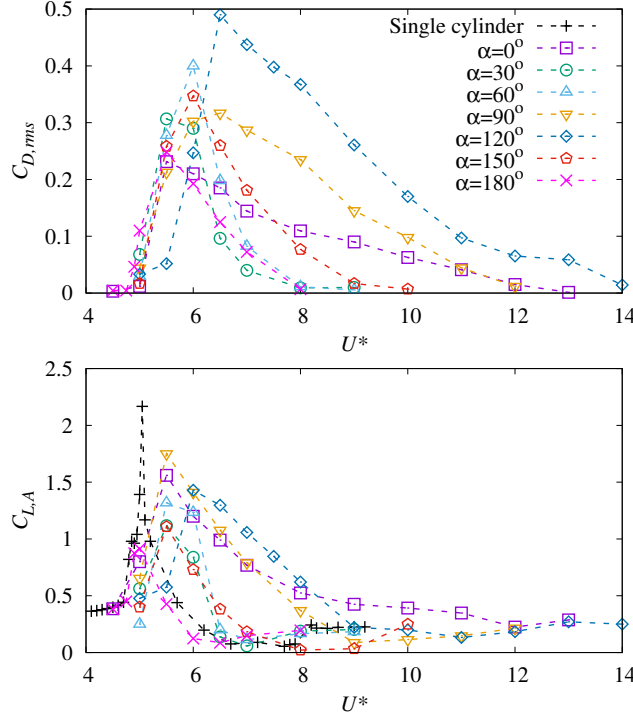

Figure 8: Root-mean-square profiles of the drag ($C_{D,rms}$) and lift amplitude ($C_{L,A}$) coefficients of the piggyback system against U^*.

$$Y(t) = A_0 + \sum_{i=1}^{\infty} A_i \sin(2\pi f_i t + \phi_i) \tag{32}$$

where f_i represents the ith frequency component. According to Eq. (13), the lift coefficient will take the following term

$$C_L(t) = \sum_{i=1}^{\infty} 2\pi^3 \left(\frac{m^* + 1}{U^{*2}} - m^* f_i^2 \right) A_i \sin(2\pi f_i t + \phi_i) + 2\pi^3 (m^* + 1) A_0 / U^{*2} \tag{33}$$

We may focus at the single component of the dominant frequency which is $f_i = f_y^*$. Then

$$A_Y = C_{L,A} \bigg/ \left| 2\pi^3 \left(\frac{m^* + 1}{U^{*2}} - m^* f_y^{*2} \right) \right| = C_{L,A} / \left(2\pi^3 m^* \left| (1.0488 f_n^*)^2 - f_y^{*2} \right| \right) \tag{34}$$

where $m^* = 10$. From the curve of f^* in Figure 6, it can be seen that f_y^* is around f_n^* at moderate U^*, which leads to that the motion amplitude A_Y may remain large even when $C_{L,A}$ is not. As U^* increases to a particular value ($U^* \approx 8.3$), $C_{L,A}$ increases again. In contrast with the single circular cylinder, the value of U^* associated with the peak of the $C_{L,A}$ of the piggyback cylinder system shifts to a larger one except at $\alpha = 180^o$, which is consistent with the shift of the U_{IU}^* to a larger U^*. At $\alpha = 0^o$, 90° and 120°, the $C_{L,A}$ curves are similar to that of the single cylinder. At other α, corresponding to the two branches of A_Y, $C_{L,A}$ first increases with U^* and then decreases after reaching the largest value at the U^* where A_Y is the largest.
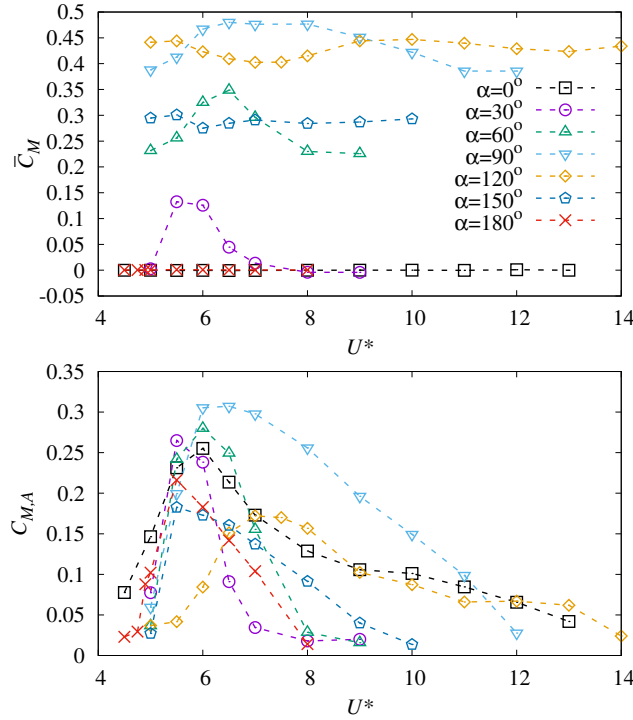

Figure 9: Mean moment coefficient ($\overline{C}_M$ and moment coefficient amplitude ($C_{M,A}$) of the piggyback cylinder system.

The mean value $\overline{C}_M$ and amplitude $C_{M,A}$ of the moment coefficient ($C_M(t)$) of the piggyback circular cylinder system are plotted in Figure 9. When $\alpha = 0^o$ and 180°, the piggyback cylinder system is symmetric about the horizontal centre line, and the mean values of the C_M are zero. For the other configurations, the piggyback cylinder system may rotate by a certain angle to reach a new mean position where the mean moment equals the moment due to the stiffness in rotation k_M^*. It is observed that $\overline{C}_M$ is positive when $\alpha \neq 0^o$ and $\alpha \neq 180^o$. Large values of $\overline{C}_M$ appear when $\alpha = 90^o$ or 120°. This implies that the system may deviate from the initial position with the relatively large angle when $\alpha = 90^o$ or 120°. The characteristics of the $C_{M,A}$ are similar to that of the $C_{L,A}$. The peaks of the $C_{M,A}$ appear in the range of $5.5 \leq U^* \leq 6.5$. $C_{M,A}$ remains significant in a relatively smaller range of U^* when $\alpha = 30^o$, 60°, 150° or 180°. $C_{M,A}$ is still significant at large U^* when $\alpha = 0^o$, 90° or 120°.
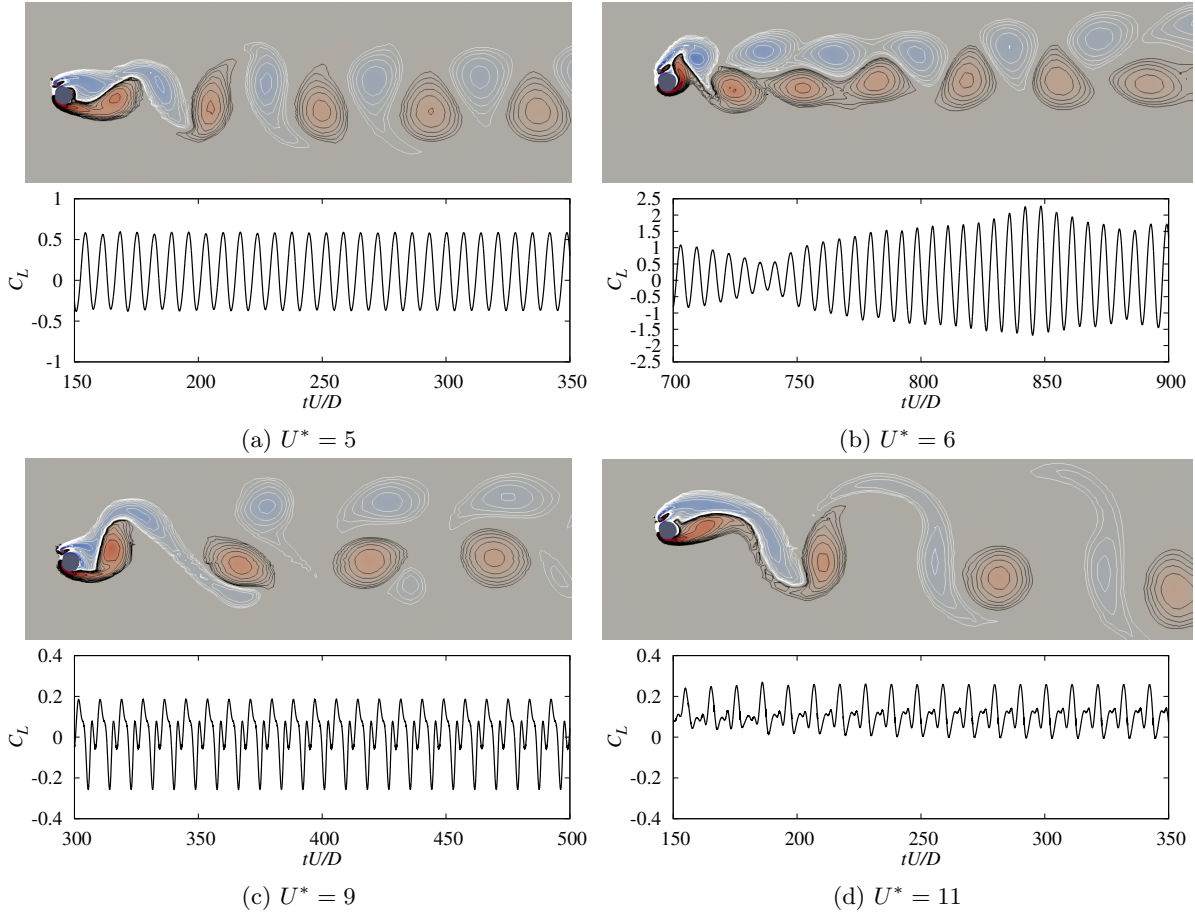
14

Figure 10: Instantaneous vorticity contours and C_L profiles of the piggyback cylinder system with $\alpha = 120^o$.

5.4. Wake flow

As described by Singh and Mittal (2005)[40], the vortex shedding in the wake of a single circular cylinder at $Re = 100$ takes "2S" mode for all U^*, in which two single vortices are alternately shed from each side of the cylinder during one vortex shedding cycle. For the present piggyback circular cylinder system with three degrees of freedom, the vortex shedding mode is found to be similar to that of the single circular cylinder when $\alpha = 0^o$, 30°, 60°, 150°, 180°. At $\alpha = 90^o$ and 120°, the wake flow patterns become different. Figure 10 shows instantaneous vorticity contours and the C_L profiles of the piggyback cylinder system with $\alpha = 120^o$ at four U^* (variations of the wake flow with U^* at $\alpha = 90^o$ and 120° are similar). In the contours, the blue color and white lines represent the negative vorticity (the clockwise vortex), the red color and black lines represent the positive vorticity (the anti-clockwise vortex). When $U^* = 5$, where the vibration amplitude is small, the "2S mode of vortex shedding is observed. According to the periodic profiles of C_L, it can be known that vortices of such "2S" mode are periodically shed downstream. When $U^* = 6$ or around U^*_{IU}, the vortices are still shed in a "2S" mode. However, the vortex shedding becomes non-periodic. When $U^* = 9$, where the largest vibration amplitude is achieved, the vortex shedding turns to a "P+S" mode, in which a pair of vortices and a single vortex are formed per cycle. When U^* increases from 9 to 11, the two clockwise vortices coalesce to form an elongated vortex.

5.5. Effect of rotation

Simulations for the rotation-constrained piggyback circular cylinder systems are also performed in the study. To account for the effect of the rotation on the motion response, in-line X_{rms} and transverse A_Y of the rotation-constrained and rotation-unconstrained piggyback cylinder systems are compared in Figure 11. It can be seen that, with the given I_{zz} and k^*_M, the X_{rms} and A_Y of the rotation-unconstrained piggyback cylinder system are larger than those of the rotation-constrained system around the resonance region when $\alpha = 0^0$, 30^0, 60^0 or 90^0. The deviations of the X_{rms} and A_Y between the two systems
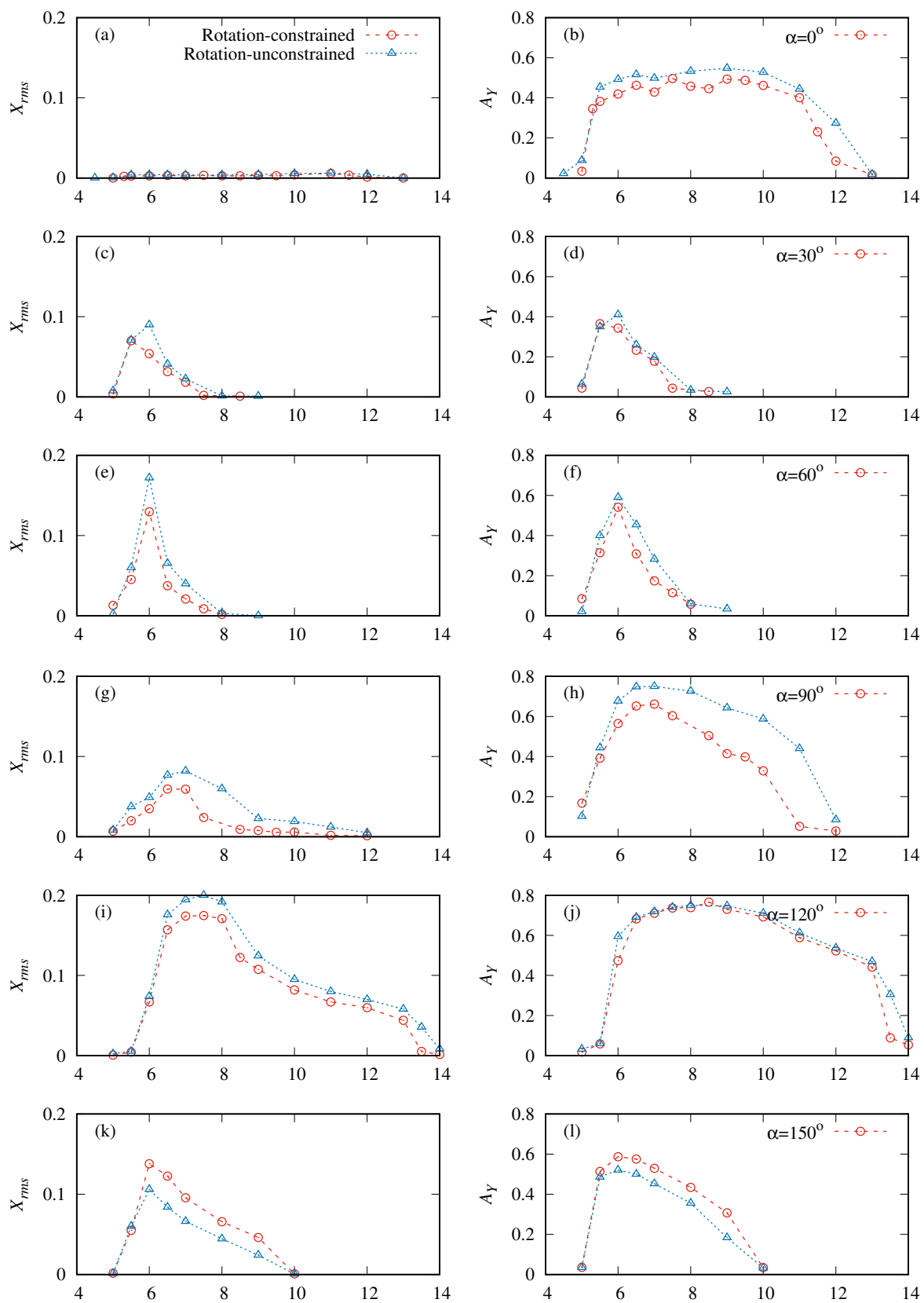
Figure 11: Comparisons of in-line X_{rms} and transverse A_Y between rotation-constrained and rotation-unconstrained piggyback cylinder systems. (Continued)
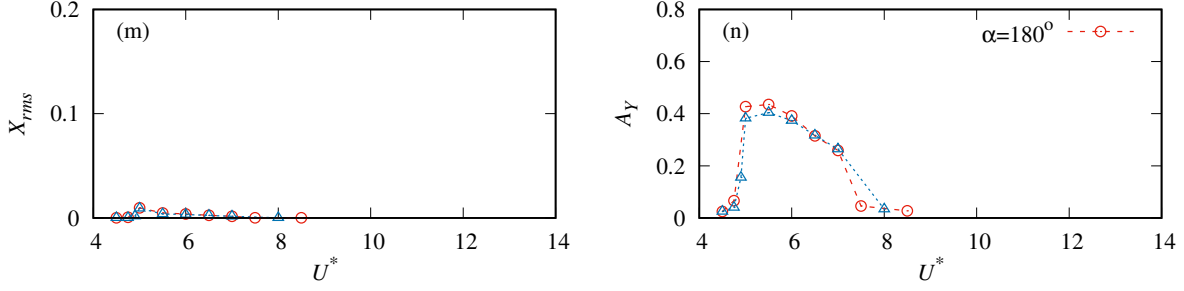
16

Figure 11: Comparisons of in-line X_{rms} and transverse A_Y between rotation-constrained and rotation-unconstrained piggyback cylinder systems.

increase with α form $\alpha = 0^0$ to 90^0. When $\alpha = 120^0$, X_{rms} of the rotation-unconstrained piggyback cylinder system is still significantly larger than that of the rotation-constrained system, and the results of A_Y from the two systems are very close to each other. As $\alpha = 150^0$ or 180^0, X_{rms} and A_Y of the rotation-unconstrained piggyback cylinder system around the resonance region are smaller than the corresponding ones of the rotation-constrained system.

Figure 12 shows time histories of the C_D, C_L, X, Y and θ of the two systems with $\alpha = 0^o$ at $U^* = 9$, where the largest transverse oscillation amplitude is achieved. At this α, the rotational motion of the piggyback cylinder system is symmetric about the horizontal centre line. Through the time histories of the C_D and C_L, it can be seen that the rotational motion leads the amplitudes of the C_D and C_L to increase somewhat. The increase of the amplitude of the C_L causes the A_Y to slightly increase, which can be seen in the profiles of Y. The mean of C_D increases slightly as well. Therefore, the mean X of the rotation-unconstrained piggyback cylinder system is larger than that of the rotation-constrained system.
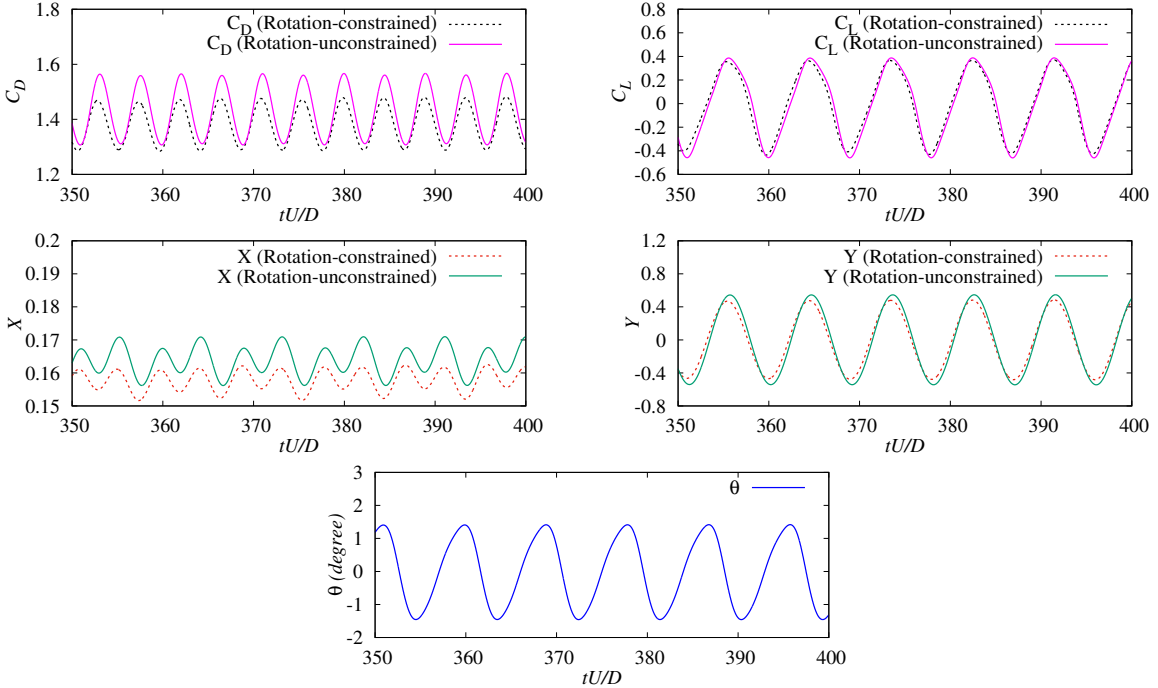

Figure 12: Time histories of the C_D, C_L, X, Y and θ of the rotation-unconstrained and rotation-constrained piggyback circular cylinder systems with $\alpha = 0^o$ at $U^* = 9$.

Figure 13 shows time histories of the C_D, C_L, X, Y and θ of the two systems with $\alpha = 90^o$ at $U^* = 7$. It is noted that the rotation angle of the system is always positive, which indicates that the rotation of the cylinder system reaches a new mean angle in the anti-clockwise direction. Therefore, the variation of the motion response of the rotation-unconstrained cylinder system is not only due to the time varying rotation itself, but also because that the system has moved to a new mean angle (around $\alpha + 5.35^o$),

17

which is equivalent to a larger α. Because of that, through the time histories, it can be seen that the amplitude of the C_L increases significantly in comparison with the rotation-constrained system, and A_Y increases correspondingly. The results also show that the amplitude of the C_D does not increase, while X_{rms} increases.
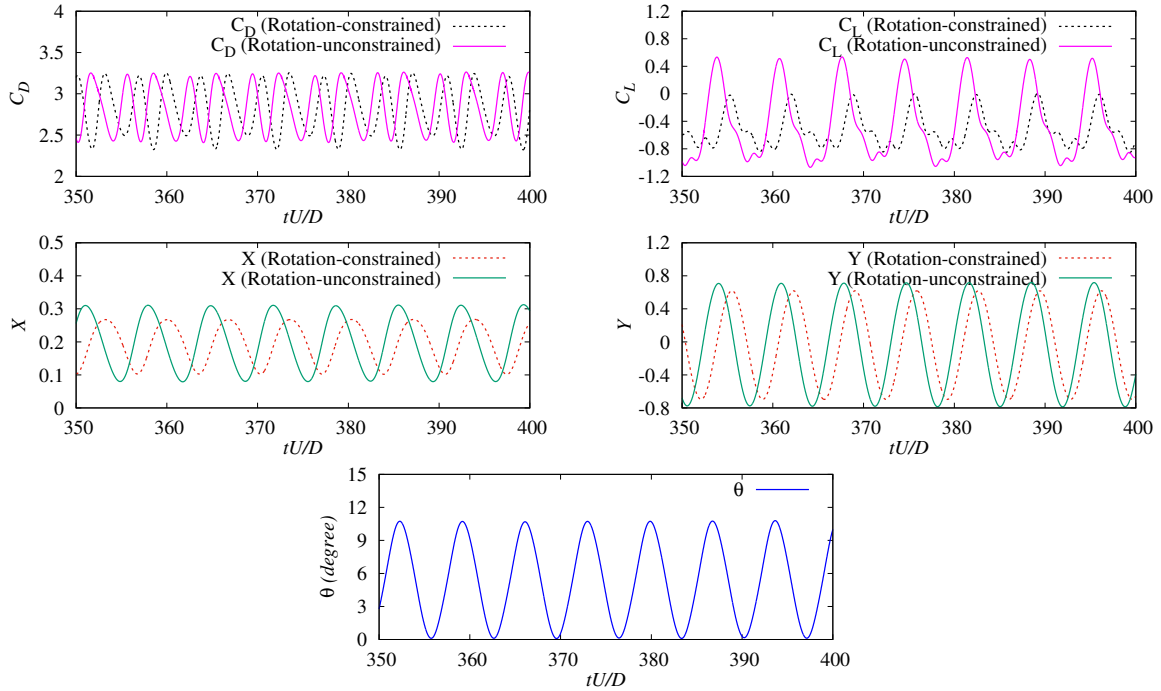

Figure 13: Time histories of the C_D, C_L, X, Y and θ of the rotation-unconstrained and rotation-constrained piggyback circular cylinder systems with $\alpha = 90^o$ at $U^* = 7$.

When $\alpha = 150^o$, the piggyback cylinder system may still move to a new angle larger than the original α. Time histories of the C_D, C_L, X, Y and θ of the two systems at $U^* = 6$ are shown in Figure 14. It can be seen that the mean θ is positive. However, the amplitudes of the C_D and C_L become smaller in this case in comparison with the rotation-constrained system. Consequently, the X_{rms}, which is related to the amplitude of X, and A_Y of the piggyback cylinder system become smaller when the rotation is unconstrained.

According to Figure 11, the X_{rms} and A_Y of the rotation-constrained system increase with α from $\alpha = 30^o$ to 120° and decrease with α from $\alpha = 120^o$ to 180°. It can be observed that the rotation-unconstrained piggyback cylinder system may always move to a larger α when $\alpha \neq 0^o$ and $\alpha \neq 180^o$ owing to the positive moment coefficient as shown in Figure 9. Therefore, the X_{rms} and A_Y of the rotation-unconstrained piggyback cylinder system may become larger from $\alpha = 30^o$ to 90° or become smaller in $120^o < \alpha < 180^o$ in comparison with those of the rotation-constrained system since it moves to the larger α. $\alpha = 120^o$ may be close to a critical value for the variation of the A_Y with α, in the sense the A_Y of the two systems coincide with each other closely when $\alpha = 120^o$.

6. Conclusions

Studies have been undertaken for the VIV of a piggyback cylinder system in three-degree-freedom based on direct numerical simulation of the Navier-Stokes equations in the arbitrary Lagrangian-Eulerian from, using a stabilized finite element method. At each time step, a generalized-α method is used for temporal derivative and the nonlinear system of the discrete equations are solved through iteration. A moving mesh is adopted. The equations of the cylinder motions are solved using a Newmark-β algorithm. From the results, the following conclusions can be drawn in the context of mass, stiffness and Reynolds chosen in the work.

1. In a steady and uniform incoming flow, after a transition period, the motion trajectory of the piggyback circular cylinder system reaches a cyclical state in most cases within the range of the reduced velocity U^* calculated, although hysteretic or non-cyclical motion may occur in some range.
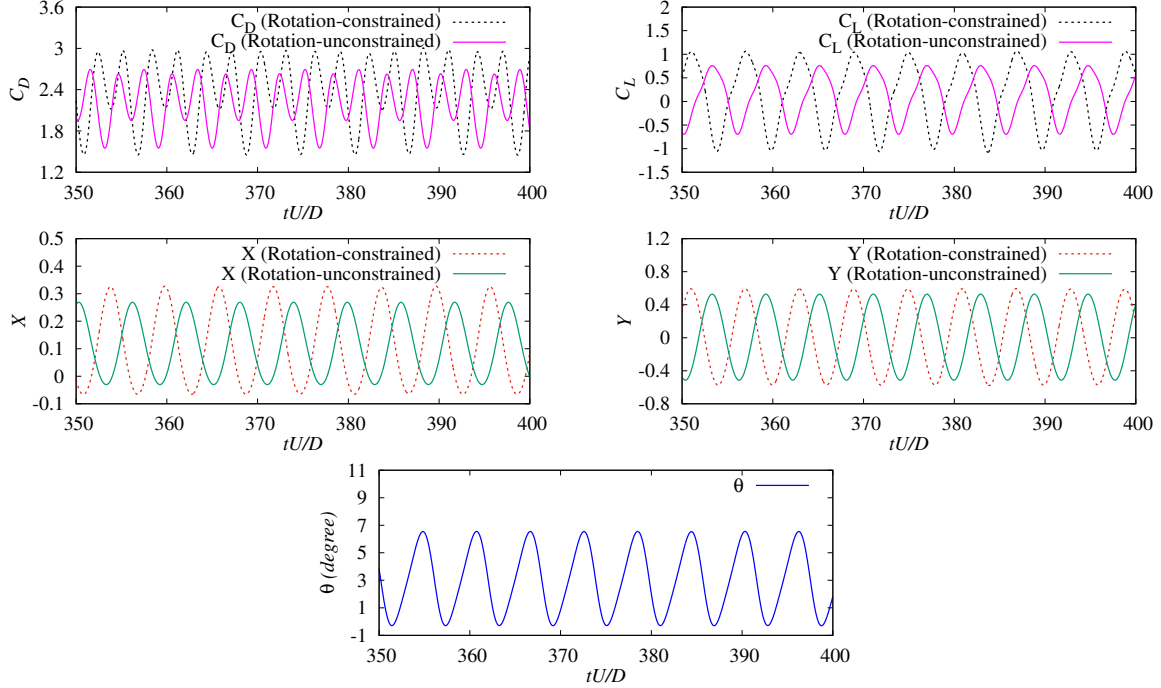
18

Figure 14: Time histories of the C_D, C_L, X, Y and θ of the rotation-unconstrained and rotation-constrained piggyback circular cylinder systems with $\alpha = 150^o$ at $U^* = 6$.

2. When the system is in tandem arrangement, or when $\alpha = 0^o$ or 180°, where α is the angle between the line linking the two centres of the cylinders and flow direction, the motion trajectories take a form of a classical pattern of 8. The motion trajectories are right-leaning closed curves when $\alpha = 30^o$ and 60°, and are left-leaning closed curves when $\alpha = 90^o$ 120° and 150°.

3. The motion amplitude curves against U^* are very much affected by α. For the amplitude of the transverse motion A_Y, when $\alpha = 0^o$, 90° and 120°, its variation from initial branch to the upper branch at U^*_{IU} is less steep than that of the single cylinder. A_Y of the piggyback cylinder is generally larger than that of the single cylinder in the upper branch, and it remains significant over a wider range of U^*. When $\alpha = 30^o$, 60°, 150° and 180°, the transverse motion is generally smaller than that of a single cylinder.

4. In comparison with the single cylinder, the ratio of the transverse (or rotational) motion frequency to the natural frequency, or $f^* = f_y^*/f_n^*$ of the piggyback cylinder is around 1 over a wider range of U^* when $\alpha = 0^o$, 90° and 120°, and over a narrower range of U^* when $\alpha = 30^o$, 60° and 180°.

5. For each α, the peak of the rotational displacement θ_A occurs at a U^* close to that corresponding to the peak of A_Y.

6. The mean of rotational displacement is positive when when $\alpha \neq 0^o$ and $\alpha \neq 180^o$, which effectively moves the alpha to a larger value. A_Y of the rotation-unconstrained piggyback system are generally larger when $\alpha = 0^o$, 30°, 60° and 90°, and is generally smaller when $\alpha < 150^o$ and 180° than that of the rotation-constrained system.

7. Acknowledgments

References

[1] Brockbank, Bundled pipe speeds offshore laying, Oil & Gas Journal 88 (1990) 78–84.

[2] S. Maddah, F. Kolahdouzan, A. Pahlavan, V. Singh, H. Afzalimehr, Experimental investigation of scouring around piggyback pipelines in different arrangements, American Journal of Environmental Engineering 11 (2021) 16–20.

[3] D. X. Fan, B. H. Wu, D. Bachina, M. Triantafyllou, Vortex-induced vibration of a piggyback pipeline half buried in the seabed, Journal of Sound and Vibration 449 (2019) 182–195.

[4] S. Kalghatgi, P. Sayer, Hydrodynamic forces on piggyback pipeline configurations, Journal of Waterway, Port, Coastal and Ocean Engineering 123 (1997) 16–22.

[5] H. Zeitoun, M. Brankovic, K. Tornes, S. Wong, E. Hollingsworth, A. Pearce, H. Sabavala, Dynamic stability response of piggyback pipelines, in: Proceedings of the ASME 2010 29th International Conference on Ocean, Offshore and Arctic Engineering, 2010, pp. 731–739.

[6] P. Strykowski, K. Sreenivasan, On the formation and suppression of vortex 'shedding' at low Reynolds numbers, Journal of Fluid Mechanics 218 (1990) 71–107.

[7] H. Sakamoto, H. Haniu, Optimum suppression of fluid forces acting on a circular cylinder, Journal of Fluids Engineering 116 (2) (1994) 221–227.

[8] T. Tsutsui, T. Igarashi, K. Kamemoto, Interactive flow around two circular cylinders of different diameters at close proximity. experiment and numerical analysis by vortex method, Journal of Wind Engineering and Industrial Aerodynamics 69-71 (1997) 279–291.

[9] C. Dalton, Y. Xu, J. Owen, The suppression of lift on a circular cylinder due to vortex shedding at moderate Reynolds numbers, Journal of Fluids and Structures 15 (3-4) (2001) 617–628.

[10] M. Zhao, L. Cheng, B. Teng, D. Liang, Numerical simulation of viscous flow past two circular cylinders of different diameters, Applied Ocean Research 27 (1) (2005) 39–55.

[11] M. Zhao, L. Cheng, B. Teng, G. Dong, Hydrodynamic forces on dual cylinders of different diameters in steady currents, Journal of Fluids and Structures 23 (1) (2007) 59–83.

[12] M. Zhao, Influence of the position angle of the small pipeline on vortex shedding flow around a sub-sea piggyback pipeline, Coastal Engineering Journal 54 (3) (2012) 1250017.

[13] Z. P. Zang, F. P. Gao, J. S. Cui, Physical modeling and swirling strength analysis of vortex shedding from near-bed piggyback pipelines, Applied Ocean Research 40 (2013) 50–59.

[14] M. Zhao, G. Yan, Numerical simulation of vortex-induced vibration of two circular cylinders of different diameters at low Reynolds number, Physics of Fluids 25 (8) (2013) 618–633.

[15] Z. P. Zang, F. P. Gao, Steady current induced vibration of near-bed piggyback pipelines: Configuration effects on VIV suppression, Applied Ocean Research 46 (2) (2014) 62–69.

[16] C. H. K. Williamson, Three-dimensional wake transition, Journal of Fluid Mechanics 328 (1996) 345–407.

[17] T. J. R. Hughes, W. K. Liu, T. K. Zimmermann, Lagrangian-Eulerian finite element formulation for incompressible viscous flows, Computer Methods in Applied Mechanics and Engineering 29 (3) (1981) 329–349.

[18] A. N. Brooks, T. J. R. Hughes, Streamline upwind/Petrov-Galerkin formulations for convection dominated flows with particular emphasis on the incompressible Navier-Stokes equations, Computer Methods in Applied Mechanics and Engineering 32 (1-3) (1982) 199–259.

[19] T. J. R. Hughes, L. P. Franca, M. Balestra, A new finite element formulation for computational fluid dynamics: V. Circumventing the Babuska-Brezzi condition: A stable Petrov-Galerkin formulation of the Stokes problem accommodating equal-order interpolations, Computer Methods in Applied Mechanics and Engineering 59 (1986) 85–99.

[20] T. E. Tezduyar, S. Mittal, S. E. Ray, R. Shih, Incompressible flow computations with stabilized bilinear and linear equal-order-interpolation velocity-pressure elements, Computer Methods in Applied Mechanics and Engineering 95 (2) (1992) 221–242.

[21] M. A. Behr, L. P. Franca, T. E. Tezduyar, Stabilized finite element methods for the velocity-pressure-stress formulation of incompressible flows, Computer Methods in Applied Mechanics and Engineering 104 (1) (1993) 31–48.

[22] T. E. Tezduyar, Finite element methods for flow problems with moving boundaries and interfaces, Archives of Computational Methods in Engineering 8 (2) (2001) 83–130.

[23] T. E. Tezduyar, Computation of moving boundaries and interfaces and stabilization parameters, International Journal for Numerical Methods in Fluids 43 (5) (2003) 555–575.

[24] L. F. Chen, G. X. Wu, Boundary shear flow past a cylinder near a wall, Applied Ocean Research 92 (2019) 101923.

[25] T. J. R. Hughes, Multiscale phenomena: Green's functions, the Dirichlet-to-Neumann formulation, subgrid scale models, bubbles and the origins of stabilized methods, Computer Methods in Applied Mechanics and Engineering 127 (1-4) (1995) 387–401.

[26] T. J. R. Hughes, G. R. Feijoo, L. Mazzei, The variational multiscale method-a paradigm for computational mechanics, Computer Methods in Applied Mechanics and Engineering 166 (1-2) (1998) 3–24.

[27] T. J. R. Hughes, G. Scovazzi, L. P. Franca, Multiscale and Stabilized Methods, John Wiley & Sons, Ltd, 2017, Ch. 2, pp. 1–64.

[28] F. Shakib, T. J. R. Hughes, Z. Johan, A new finite element formulation for computational fluid dynamics: X. The compressible Euler and Navier-Stokes equations, Computer Methods in Applied Mechanics and Engineering 89 (1-3) (1991) 141–219.

[29] C. Taylor, T. Hughes, C. Zarins, Finite element modeling of blood flow in arteries, Computer Methods in Applied Mechanics and Engineering 158 (158) (1998) 155–196.

[30] Y. Bazilevs, V. M. Calo, T. J. R. Hughes, Y. Zhang, Isogeometric fluid-structure interaction: Theory, algorithms, and computations, Computational Mechanics 43 (1) (2008) 3–37.

[31] F. Shakib, Finite element analysis of the compressible Euler and Navier-Stokes equations, Ph.D. thesis, Stanford University (1989).

[32] G. X. Wu, Z. Z. Hu, Numerical simulation of viscous flow around unrestrained cylinders, Journal of Fluids and Structures 22 (3) (2006) 371–390.

[33] K. Jansen, C. Whiting, G. Hulbert, A generalized-α method for integrating the filtered Navier-Stokes equations with a stabilized finite element method, Computer Methods in Applied Mechanics and Engineering 190 (3-4) (2000) 305–319.

[34] L. F. Chen, G. X. Wu, Flow-induced transverse vibration of a circular cylinder close to a plane wall at small gap ratios, Applied Ocean Research 103 (2020) 102344.

[35] L. Chen, Y. Dong, Y. Wang, Flow-induced vibration of a near-wall circular cylinder with a small gap ratio at low Reynolds numbers, Journal of Fluids and Structures 103 (1) (2021) 103247.

[36] T. K. Prasanth, S. Behara, S. P. Singh, R. Kumar, S. Mittal, Effect of blockage on vortex-induced vibrations at low Reynolds numbers, Journal of Fluids and Structures 22 (6-7) (2006) 865–876.

[37] Y. Bazilevs, C. Michler, V. Calo, T. Hughes, Isogeometric variational multiscale modeling of wall-bounded turbulent flows with weakly enforced boundary conditions on unstretched meshes, Computer Methods in Applied Mechanics

20

and Engineering 199 (13-16) (2010) 780–790.

[38] L. F. Chen, S. J. Hulshoff, Y. T. Wang, 2d residual-based les of flow around a pipeline close to a flat seabed, Computer Methods in Applied Mechanics and Engineering 363 (2020) 112788.

[39] L. F. Chen, Y. T. Wang, S. Y. Sun, S. Q. Wang, The effect of boundary shear flow on hydrodynamic forces of a
445   pipeline over a fully scoured seabed, Ocean Engineering 206 (2020) 107326.

[40] S. P. Singh, S. Mittal, Vortex-induced oscillations at low Reynolds numbers: Hysteresis and vortex-shedding modes, Journal of Fluids and Structures 20 (8) (2005) 1085–1104.

[41] H. Jiao, G. X. Wu, Analysis of fluctuating force acting on two cylinders in different arrangements through Lattice Boltzmann method, Journal of Fluids and Structures 82 (2018) 101–120.

450   [42] A. Khalak, C. H. K. Williamson, Fluid forces and dynamics of a hydroelastic structure with very low mass and damping, Journal of Fluids and Structures 11 (8) (1997) 973–982.

[43] H. Jiao, G. X. Wu, Effect of Reynolds number on amplitude branches of vortex-induced vibration of a cylinder, Journal of Fluids and Structures 105 (3) (2021) 103323.